

# Uformer-ICS: A Specialized U-Shaped Transformer for Image Compressive Sensing

Kuiyuan Zhang, Zhongyun Hua, Yuanman Li, Yushu Zhang,  
Yicong Zhou, *Senior Member, IEEE*

**Abstract**—Recently, several studies have applied deep convolutional neural networks (CNNs) in image compressive sensing (CS) tasks to improve reconstruction quality. However, convolutional layers generally have a small receptive field; therefore, capturing long-range pixel correlations using CNNs is challenging, which limits their reconstruction performance in image CS tasks. Considering this limitation, we propose a U-shaped transformer for image CS tasks, called the Uformer-ICS. We develop a projection-based transformer block by integrating the prior projection knowledge of CS into the original transformer blocks, and then build a symmetrical reconstruction model using the projection-based transformer blocks and residual convolutional blocks. Compared with previous CNN-based CS methods that can only exploit local image features, the proposed reconstruction model can simultaneously utilize the local features and long-range dependencies of an image, and the prior projection knowledge of the CS theory. Additionally, we design an adaptive sampling model that can adaptively sample image blocks based on block sparsity, which can ensure that the compressed results retain the maximum possible information of the original image under a fixed sampling ratio. The proposed Uformer-ICS is an end-to-end framework that simultaneously learns the sampling and reconstruction processes. Experimental results demonstrate that it achieves significantly better reconstruction performance than existing state-of-the-art deep learning-based CS methods.

**Index Terms**—Compressive sensing, image reconstruction, adaptive sampling, deep learning, transformer

## I. INTRODUCTION

Compressive sensing (CS) is an effective signal acquisition technique that can reconstruct a signal using its compressed measurements, which are significantly less than the measurements required by the Nyquist sampling theorem [1], [2]. The sampling process for a signal  $\mathbf{x} \in \mathbb{R}^{n \times 1}$  can be expressed as  $\mathbf{y} = \Phi \mathbf{x}$ , where  $\mathbf{y} \in \mathbb{R}^{m \times 1}$  comprises the compressed

measurements and  $\Phi \in \mathbb{R}^{m \times n}$  is a measurement matrix wherein  $n \gg m$ . Because the CS technique can achieve a high compression ratio while maintaining a high reconstruction quality, it can be potentially used in numerous signal acquisition and compression applications [3], especially for tasks involving image signals with high data redundancy [4]. The reconstruction process of CS involves finding solutions for an underdetermined linear system. To achieve high efficiency and accurate reconstruction results, most traditional CS reconstruction algorithms use nonlinear iterations to reconstruct the original signal [5]–[8], which is extremely time-consuming. Therefore, these traditional CS methods may not be suitable for real-time applications. Additionally, these traditional CS methods cannot achieve a high reconstruction quality because they lack adaptability to sample signals with varying characteristics.

Some deep learning-based image CS methods have been developed that can achieve both high reconstruction quality and efficiency [9]–[13]. These deep learning-based image CS methods use convolutional neural networks (CNNs) to replace the time-consuming iterative reconstruction process in traditional CS algorithms. They adaptively learn the measurement matrix and reconstruction network using a massive amount of training data. To maintain theoretical interpretability, some of them unfold the traditional CS algorithms into their CS networks using CNNs [11], [13]. However, nearly all existing deep learning-based image CS methods are developed using CNNs. Owing to the spatial invariance and local inductive biases, CNNs cannot effectively capture long-range dependencies. This results in a limitation to these deep learning-based image CS methods. Moreover, the sparsity in different areas of a natural image usually varies, and most deep learning-based image CS methods sample all image areas using the same sampling ratio without appropriately considering the uneven sparsity distribution.

The transformer has been extremely successful in natural language processing tasks owing to the robust ability of its self-attention mechanism for capturing long-range dependencies among input tokens [14]. Recently, several studies have successfully extended the transformer architecture to various computer vision tasks [15]–[18] and obtained significant performance improvements over previous CNN-based methods. These studies have demonstrated that the long-range dependencies are extremely useful for improving the feature modeling ability of networks. Therefore, introducing the long-range dependency capturing ability of the transformer in image CS tasks is helpful for improving the reconstruction

This work was supported in part by the National Natural Science Foundation of China under Grants 62071142 and 62001304, by the Guangdong Basic and Applied Basic Research Foundation under Grants 2021A1515011406 and 2022A1515010645, by the Shenzhen College Stability Support Plan under Grant GXWD20201230155427003-20200824210638001, by the Foundation for Science and Technology Innovation of Shenzhen under Grant RCBS20210609103708014.

Kuiyuan Zhang and Zhongyun Hua are with School of Computer Science and Technology, Harbin Institute of Technology, Shenzhen, Shenzhen 518055, China (e-mail: zkyhitsz@gmail.com; huazyum@gmail.com).

Yuanman Li is with College of Electronics and Information Engineering, Shenzhen University, Shenzhen 518060, China (e-mail: yuanmanli@szu.edu.cn)

Yushu Zhang is with the College of Computer Science and Technology, Nanjing University of Aeronautics and Astronautics, Nanjing, Jiangsu 210016, China (e-mail: yushu@nuaa.edu.cn).

Yicong Zhou is with Department of Computer and Information Science, University of Macau, Macau 999078, China (e-mail: yicongzhou@um.edu.mo).

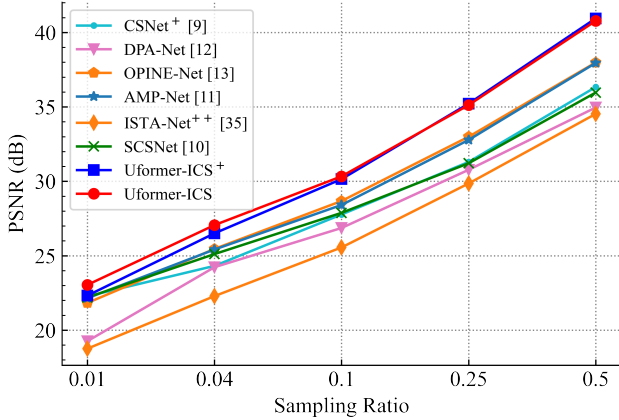


Fig. 1. Reconstruction performances of the proposed and existing state-of-the-art deep learning-based CS methods. The peak signal-to-noise ratio (PSNR) scores shown are averaged over all images in the five test datasets: Set5, Set11, Set14, BSD100, and Urban100. It is evident that the proposed method achieves significantly better PSNR scores than state-of-the-art deep learning-based CS methods.

performance.

In this paper, we propose a specialized U-shaped transformer architecture for image CS called the Uformer-ICS, and it is the first network to effectively integrate the CS theory into the transformer model, instead of simply applying the transformer to CS tasks. From an overall perspective, the Uformer-ICS comprises an adaptive sampling model and a reconstruction model. The adaptive sampling model allocates fewer sampling resources to the image block with higher sparsity while allocating more sampling resources to that with lower sparsity. Specifically, the sampling resources are linearly allocated based on block sparsity, which is measured using the saliency information. The input image is then adaptively sampled block-by-block using a single learnable measurement matrix. This sampling strategy can ensure that the compressed measurements contain the maximum possible information of the original image under a fixed sampling ratio. The reconstruction model primarily comprises projection-based transformer and residual convolutional blocks. Each projection-based transformer block is constructed by integrating the prior projection knowledge of CS into the original stacked transformer blocks. Because the projection-based transformer blocks can capture the long-range dependencies of an image and utilize the prior projection knowledge of the CS theory, and the residual convolutional blocks can exploit the local image features, the proposed reconstruction model can reconstruct the details of the original image better than the existing methods. Fig. 1 shows that the proposed Uformer-ICS achieves a better reconstruction performance than existing state-of-the-art deep learning-based CS methods.

The main contributions of this study are as follows:

- We propose a new transformer-based network for image CS, called the Uformer-ICS, which comprises an adaptive sampling model and a symmetrical reconstruction model, and is the first network to effectively integrate the CS theory into the transformer architecture.
- We design an adaptive sampling mode to linearly allocate sampling resources to image blocks based on block spar-

sity. The image block with a higher sparsity is allocated fewer sampling resources, whereas that with a lower sparsity is allocated more sampling resources.

- We develop a symmetrical reconstruction model using projection-based transformer and residual convolutional blocks, wherein each projection-based transformer block is constructed by integrating the prior projection knowledge of CS into the original transformer blocks.
- We conduct extensive experiments to evaluate the proposed Uformer-ICS. The comparison results demonstrate that it outperforms existing state-of-the-art deep learning-based CS methods, and the ablation studies validate the effectiveness of the proposed adaptive sampling strategy and the projection-based transformer block.

The rest of this paper is organized as follows. Section II reviews the traditional CS methods, deep learning-based CS methods, and vision transformers. Section III presents the network structure of the proposed Uformer-ICS. Section IV evaluates the performance of the proposed method and compares it with state-of-the-art methods. Section V conducts ablation studies. Finally, conclusions are drawn in Section VI.

## II. RELATED WORK

In this section, we present some knowledge of the traditional CS methods, and review existing deep learning-based CS methods and vision transformers.

### A. Traditional CS

1) *Block-Based CS*: The size of the measurement matrix in CS is calculated by multiplying the lengths of the input signal and output measurements. When directly sampling the 1D vector form of a 2D image, the required measurement matrix is considerably large, which results in significantly high memory and computational requirements for the sampling operation. To address this issue, traditional CS algorithms usually sample an image block-by-block [7]. Suppose that each image block  $\mathbf{x}_i$  is of size  $B \times B$  and the measurement matrix is  $\Phi_B \in \mathbb{R}^{n_B \times B^2}$ . The sampling process is expressed as

$$\mathbf{y}_i = \Phi_B \cdot \mathfrak{T}(\mathbf{x}_i), \quad (1)$$

where  $\mathfrak{T}(\mathbf{x}_i)$  denotes the 1D vector form of the image block  $\mathbf{x}_i$  and  $\mathbf{y}_i \in \mathbb{R}^{n_B \times 1}$  are the measurements of  $\mathbf{x}_i$ . The sampling ratio ( $sr$ ) is defined as  $sr = n_B/B^2$ . Generally, an image block with higher sparsity requires fewer measurements for reconstruction [19]. Therefore, some traditional CS methods improve the reconstruction quality by allocating sampling resources to different blocks [20], [21].

2) *Signal Reconstruction*: To effectively reconstruct the original signal, some traditional CS methods have developed iterative reconstruction schemes to solve the following optimization problem:

$$\min_{\hat{\mathbf{x}}_i} \frac{1}{2} \|\Phi_B \mathfrak{T}(\hat{\mathbf{x}}_i) - \mathbf{y}_i\|_2^2 + \mathfrak{R}(\hat{\mathbf{x}}_i), \quad (2)$$

where  $\mathfrak{R}(\hat{\mathbf{x}}_i)$  denotes the hand-crafted prior term regarding the structure of the original signal [5], [6], [8], [22]. Each iteration operation includes the following operations:

- **Projection onto the convex set.** Given the current reconstruction result  $\hat{\mathbf{x}}_i^t$  of  $\mathbf{x}_i$ , this operation uses the gradient descent method to minimize  $\|\Phi_B \mathfrak{T}(\hat{\mathbf{x}}_i) - \mathbf{y}_i\|_2^2$  in Eq. (2). Therefore, it can find a vector closer to the hyperplane  $\mathbf{H} = \{\hat{\mathbf{x}}_i : \Phi_B \mathfrak{T}(\hat{\mathbf{x}}_i) = \mathbf{y}_i\}$  than  $\hat{\mathbf{x}}_i^t$  without a constraint, e.g., sparsity constraint. Specifically, the projection operation is calculated as follows:

$$\mathfrak{T}(\hat{\mathbf{x}}_i^{(t+1)}) = \mathfrak{T}(\hat{\mathbf{x}}_i^{(t)}) + \alpha \Phi_B^T(\mathbf{y}_i - \Phi_B \mathfrak{T}(\hat{\mathbf{x}}_i^{(t)})), \quad (3)$$

where  $t$  indicates the iteration step,  $\Phi_B^T(\mathbf{y}_i - \Phi_B \mathfrak{T}(\hat{\mathbf{x}}_i^{(t)}))$  denotes the gradient of  $\|\Phi_B \mathfrak{T}(\hat{\mathbf{x}}_i) - \mathbf{y}_i\|_2^2$  in Eq. (2), and  $\alpha$  is the updating step length.

- **Optimizing the prior term.** This operation aims to minimize the hand-crafted prior term  $\mathfrak{R}(\hat{\mathbf{x}}_i)$  to constrain the current reconstruction result  $\hat{\mathbf{x}}_i^{(t+1)}$ . For example, the iterative shrinkage-thresholding algorithm (ISTA) [5] and approximate message passing algorithm (AMP) [22] set the  $l_1$  norm as the prior term to constrain the signal sparsity, and use a shrinkage/thresholding non-linearity to process  $\hat{\mathbf{x}}_i^{(t+1)}$ . The denoising-based AMP (DAMP) [23] assumes that the original signal belongs to a certain image class  $\mathcal{C}$ , and uses a denoiser to project  $\hat{\mathbf{x}}_i^{(t+1)}$  onto  $\mathcal{C}$ .

Despite having good interpretability, traditional CS algorithms suffer from poor reconstruction performance and low efficiency because they cannot adaptively learn the features of the original signal.

### B. Deep Learning-Based CS

In 2015, the authors of [24] used a deep learning method to solve the signal reconstruction problem and proposed a stacked denoising auto-encoder to reconstruct image patches from their measurements. Inspired by the application of CNNs in image restoration tasks, Kulkarni *et al.* [25] proposed a deep CNN-based model to implement the non-iterative reconstruction process. These two deep learning-based CS methods directly reconstruct image patches from their measurements [24], [25]. To further improve the reconstruction performance, Shi *et al.* proposed two end-to-end deep CNN-based models in [9], [26] for image CS, which can simultaneously learn both the sampling and reconstruction processes.

The above CS models directly regard the reconstruction process as a deep learning task without considering the characteristics of CS theory. To improve the interpretability, some studies [11], [13], [27] designed CS networks by unfolding traditional CS algorithms using CNNs. For example, inspired by the traditional ISTA method [5], Zhang *et al.* [27] proposed a deep network called ISTA-Net by solving the proximal mapping associated with the sparsity-inducing regularizer using nonlinear transformation. The authors of [11] proposed a denoising-based deep CS network called AMP-Net, wherein the reconstruction network unfolds the iterative denoising process of the AMP algorithm [22] and integrates deblocking modules to eliminate the blocking artifacts.

These existing deep learning-based CS methods use CNNs to develop reconstruction models and achieve better reconstruction performance than traditional CS methods. However,

convolutional layers in CNNs have local receptive fields and cannot effectively capture the long-range pixel correlations in image CS tasks, resulting in a limitation for achieving higher reconstruction quality.

### C. Vision Transformer

In 2017, the authors of [14] first proposed the transformer for natural language processing tasks. Compared with previous methods based on recurrent neural networks, the transformer has a more powerful ability to model long-range dependencies among tokens using the self-attention mechanism; thus, it can achieve significantly better accuracy and scalability. Specifically, the self-attention layer computes the key-query dot-product among all input tokens. Therefore, its computation complexity grows quadratically with an increase in the number of tokens [14]. When applying self-attention layers to the image-based tasks, the complexity is  $\mathcal{O}(W^2H^2)$  for an input image of size  $H \times W$ .

To handle high-resolution images, Vaswani *et al.* [15] proposed the vision transformer (ViT) that divides an image into non-overlapping patches and employs the transformer to capture dependencies among image patches for image classification tasks. In some low-level vision tasks (e.g., image denoising and image deblocking), an image may be divided into numerous patches, making the computational complexity of ViT extremely high and unacceptable. Considering this, Liu *et al.* [28] designed a shifted window-based transformer, which applies self-attention in each image window and uses shifted window partitioning to bring connections across windows. Moreover, Zamir *et al.* [29] proposed a transposed attention scheme that computes the attention map across feature channels. These efforts [28], [29] have significantly reduced the computational complexity of the transformer for image processing tasks, achieving a linear relationship between the computational complexity and the image size.

Although the transformer has shown excellent performance in many low-level vision tasks [16]–[18], [28], [29], it may not obtain a good performance if it is directly applied to the image CS tasks. This is because the image CS follows strict theoretical requirements and has some inner characteristics (e.g., adaptive sampling and projection), which are crucial for image reconstruction [11], [13], [21]. Therefore, it is necessary to integrate the prior knowledge of image CS into the transformer architecture when applying the transformer into the image CS tasks.

## III. UFORMER-ICS

This section details the proposed Uformer-ICS. From an overall perspective, the Uformer-ICS comprises an adaptive sampling model and a reconstruction model. The adaptive sampling model adaptively samples the image block-by-block using a single learnable measurement matrix, and the reconstruction model is a symmetrical U-shaped architecture that reconstructs the original image from the measurements.

To illustrate the sampling and reconstruction processes, we assume that the input image is a single-channel image that is denoted as  $\mathbf{X} \in \mathbb{R}^{H \times W \times 1}$ , and the block size is  $B \times B \times 1$ . The

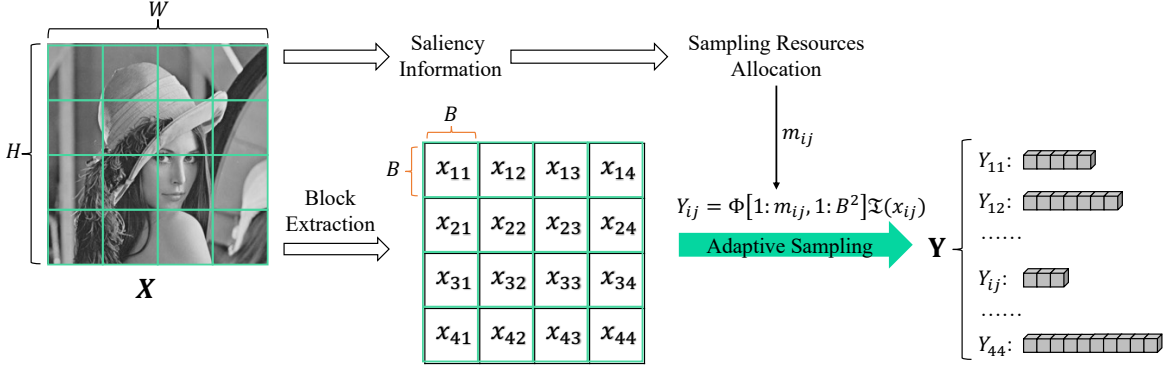


Fig. 2. Adaptive sampling model of the proposed Uformer-ICS. First, the saliency information is calculated to estimate the block sparsity, which is used to adaptively allocate sampling resources for each block. Then, the input image  $\mathbf{X}$  is adaptively sampled block-by-block using a single measurement matrix  $\Phi$ .

vector form of each image block  $\mathbf{x}_{ij}$  is represented as  $\mathfrak{T}(\mathbf{x}_{ij}) \in \mathbb{R}^{B^2 \times 1}$ . Herein,  $i = \{1, 2, \dots, h\}$  and  $j = \{1, 2, \dots, w\}$ , where  $h = \frac{H}{B}$  and  $w = \frac{W}{B}$ .

### A. Adaptive Sampling Model

The adaptive sampling process is shown in Fig. 2. It first uses the saliency information [19] to estimate the sparsity of each image block and then adaptively samples the image block-by-block according to the block sparsity.

1) *Sparsity Estimation*: Because different image blocks have different sparsity, the compressed measurements cannot contain the maximum information of the original image if all image blocks are sampled at a same sampling ratio. Generally speaking, an image block with higher sparsity should be allocated less sampling resources because it contains less information. In the proposed sampling model, the sampling resources are allocated based on the block sparsity, and the saliency information [19] is used to estimate the block sparsity. The saliency map  $\mathbf{S}$  of the input image  $\mathbf{X}$  is calculated as

$$\begin{aligned} \mathbf{P} &= \text{sign}(\mathbf{C}_t(\mathbf{X})), \\ \mathbf{F} &= \text{abs}(\mathbf{C}_t^{-1}(\mathbf{P})), \\ \mathbf{S} &= \mathbf{G} * \mathbf{F}^2, \end{aligned} \quad (4)$$

where  $\mathbf{C}_t$  denotes the 2D discrete cosine transform (DCT),  $\mathbf{C}_t^{-1}$  indicates the inverse DCT, and  $\mathbf{G}$  is a 2D Gaussian low-pass filter used to smoothen the saliency results. For each image block  $\mathbf{x}_{ij}$  and its corresponding region  $\mathbf{S}_{\mathbf{x}_{ij}}$ , the saliency information  $\mathbf{V}_{ij}$  of  $\mathbf{x}_{ij}$  is defined as

$$\mathbf{V}_{ij} = \sum_{s \in \mathbf{S}_{\mathbf{x}_{ij}}} s / \sum_{s \in \mathbf{S}} s, \quad (5)$$

where the sum of all elements in  $\mathbf{V}$  is 1.

2) *Adaptive Sampling*: An image block with less saliency information is regarded as sparser and should be allocated less sampling resources. Algorithm 1 describes the process of allocating sampling resources. First, the total number of measurements under a fixed sampling ratio are calculated and then a basic measurement number is set for each image block. This basic measurement number can ensure that some image blocks with extremely less saliency information can also be allocated a certain amount of sampling resources. The

---

### Algorithm 1 Sampling resources allocation.

---

**Input:** Saliency information  $\mathbf{V}$ , target sampling ratio  $sr_t$ , image size  $H \times W$ , block size  $B$

**Output:** measurement number  $\mathbf{m}_{ij}$

- 1:  $h, w = H/B, W/B$
  - 2:  $total = \lfloor sr_t \times H \times W \rfloor$
  - 3:  $base = \lfloor sr_t * B^2 * \beta \rfloor$
  - 4:  $rest = total - (base \times h \times w)$
  - 5: **for**  $i = 1 : h$  **do**
  - 6:     **for**  $j = 1 : w$  **do**
  - 7:          $\mathbf{m}_{ij} = base + \text{round}(rest \times \mathbf{V}_{ij})$
  - 8:     **end for**
  - 9: **end for**
- 

remaining sampling resources are linearly assigned based on the saliency information, and the final measurement number  $\mathbf{m}_{ij} \in (1, B^2]$  is obtained for each image block  $\mathbf{x}_{ij}$ .

We use a parameter  $\beta$  in Algorithm 1 to adjust the basic measurement number for various target sampling ratios. This number linearly increases with the increase in target sampling ratio when the  $\beta$  is constant. However, this process may weaken the effect of the allocation strategy. Therefore, we set the  $\beta$  to gradually decay with the increase in the target sampling ratio  $sr_t$ . Specifically, the  $\beta$  is set as

$$\beta = \begin{cases} 0.8, & sr_t < 0.1 \\ 0.9 - sr, & 0.1 \leq sr_t \leq 0.5 \end{cases} \quad (6)$$

When  $sr_t > 0.5$ , the basic measurement number does not change.

To better illustrate the adaptive sampling mechanism, we provide two examples of the measurements allocations for the ‘‘Parrots’’ and ‘‘Cameraman’’ images shown in Fig. 3. The block size is set to  $32 \times 32$ , and the number on the image block denotes the measurement number. It is evident that image blocks with more complex structures are considered to have less sparsity and are allocated more measurements. For example, the eye in the ‘‘Parrots’’ and the camera in the ‘‘Cameraman’’ contain more details and more complex structures; thus, the corresponding image blocks of these two areas are allocated more sampling resources.

Because different image blocks are allocated different measurement numbers, generating a measurement matrix for each



Fig. 3. Measurements allocations for the “Parrots” and “Cameraman” images at the sampling ratios of 0.1 and 0.25, respectively.

possible measurement number results in a significant number of parameters and extremely high memory occupation. To address this problem, we use a scalable sampling strategy that requires only one learnable measurement matrix to sample all image blocks with different measurement numbers. Assume that the learnable measurement matrix is  $\Phi \in \mathbb{R}^{B^2 \times B^2}$ , then the sampling process for each image block is as follows:

$$\mathbf{y}_{ij} = \Phi[1 : \mathbf{m}_{ij}, :] \cdot \mathcal{I}(\mathbf{x}_{ij}), \quad (7)$$

where  $\mathbf{y}_{ij} \in \mathbb{R}^{\mathbf{m}_{ij} \times 1}$  is the measurements of the image block  $\mathbf{x}_{ij}$ . We denote the collection of all measurements  $\mathbf{y}_{ij}$  as  $\mathbf{Y}$ .

### B. Reconstruction Model

The overall structure of the reconstruction model is illustrated in Fig. 4. First, the initialization value  $\mathbf{X}_0 \in \mathbb{R}^{H \times W \times 1}$  of the input image  $\mathbf{X}$  is generated by linearly mapping the measurements  $\mathbf{Y}$  directly. Specifically, the initialization process is calculated as

$$\begin{aligned} \mathcal{I}(\hat{\mathbf{x}}_{ij}) &= \Psi[:, 1 : \mathbf{m}_{ij}] \cdot \mathbf{y}_{ij} \\ \mathbf{X}_0 &= \Xi(\{\hat{\mathbf{x}}_{ij}\}) \end{aligned} \quad (8)$$

where  $\Psi \in \mathbb{R}^{B^2 \times B^2}$  represents the learnable linear mapping matrix, and  $\Xi$  denotes the pixel shuffle operation [30] that combines and transforms all linear mapping results into an image-like feature  $\mathbf{X}_0$ .

Next, the initialization  $\mathbf{X}_0$  is processed using a head module  $H_{head}$  to extend the channels and extract the local shadow features  $\mathbf{X}_h \in \mathbb{R}^{H \times W \times C_0}$ . The Uformer module then captures the long-range features from  $\mathbf{X}_h$  to obtain  $\mathbf{X}_u$ . Finally, a tail module  $H_{tail}$  aggregates the features of  $\mathbf{X}_u$  to produce a residual reconstruction result, and the final reconstruction

result  $\hat{\mathbf{X}}$  is generated by adding the initialization  $\mathbf{X}_0$  and the residual reconstruction result.

In the subsequent subsections, the head and tail modules are first illustrated and then the Uformer module is described in detail.

### C. Head & Tail Modules

As shown in Fig. 4, the head module  $H_{head}$  comprises several convolutional layers and a residual convolutional block. After obtaining the initialization result  $\mathbf{X}_0$ , the  $H_{head}$  enlarges the channels further and extracts local shallow features from  $\mathbf{X}_0$  as follows:

$$\mathbf{X}_h = H_{head}(\mathbf{X}_0), \quad (9)$$

where  $\mathbf{X}_h$  is of size  $H \times W \times C_0$ .

To ensure symmetry with the head module  $H_{head}$ , the tail module  $H_{tail}$  stacks a residual convolutional block and several convolutional layers. Given output  $\mathbf{X}_u$  of the Uformer module, the  $H_{tail}$  aggregates the features of  $\mathbf{X}_u$  to obtain the final reconstruction result  $\hat{\mathbf{X}}$  as follows:

$$\hat{\mathbf{X}} = H_{tail}(\mathbf{X}_u) + \mathbf{X}_0, \quad (10)$$

where  $\hat{\mathbf{X}}$  is of size  $H \times W \times 1$ , and the residual learning [31] is applied to improve the convergence speed and reconstruction performance of the proposed model.

### D. Uformer

As illustrated in Fig. 4, the Uformer is a U-shaped four-level hierarchical encoder-decoder. To introduce the prior knowledge of CS into the transformer architecture, we propose a multi-channel projection and integrate it into the stacked transformer blocks to develop the projection-based transformer block. In the following sections, we will illustrate the overall pipeline of the Uformer and present its components in detail.

1) *Pipeline*: Based on the common design of the U-shaped structure [32], the output  $\mathbf{X}_h$  of the head module is first passed through four encoder levels. The resolutions of feature maps are gradually reduced from the top to the bottom levels using feature down-sampling operations shown in Fig. 5 (a). We employ a  $3 \times 3$  convolutional layer and pixel unshuffle operation [30] to double the number of channels and reduce the resolution by 50%. Therefore, the  $i$ -th level of the encoder produces a feature map of size  $\frac{H}{2^i} \times \frac{W}{2^i} \times 2^i C_0$ , where  $i \in [0, 1, 2, 3]$ .

The decoder progressively recovers the high-resolution features by using the low-resolution feature map from the lowest encoder level as its input. Fig. 5 (b) shows the feature up-sampling operation. We employ a  $3 \times 3$  convolutional layer and pixel shuffle operation [30] to reduce the channels by 50% and double the resolution. Moreover, the features obtained on the decoder side are fused with the encoder features to enhance the feature representation.

2) *Window-Based Self-attention*: The computational complexity of the original self-attention layer in the transformer increases quadratically with image size. In this study, the window-based multi-head self-attention (W-MSA) [28] is used to reduce the computational complexity because it computes

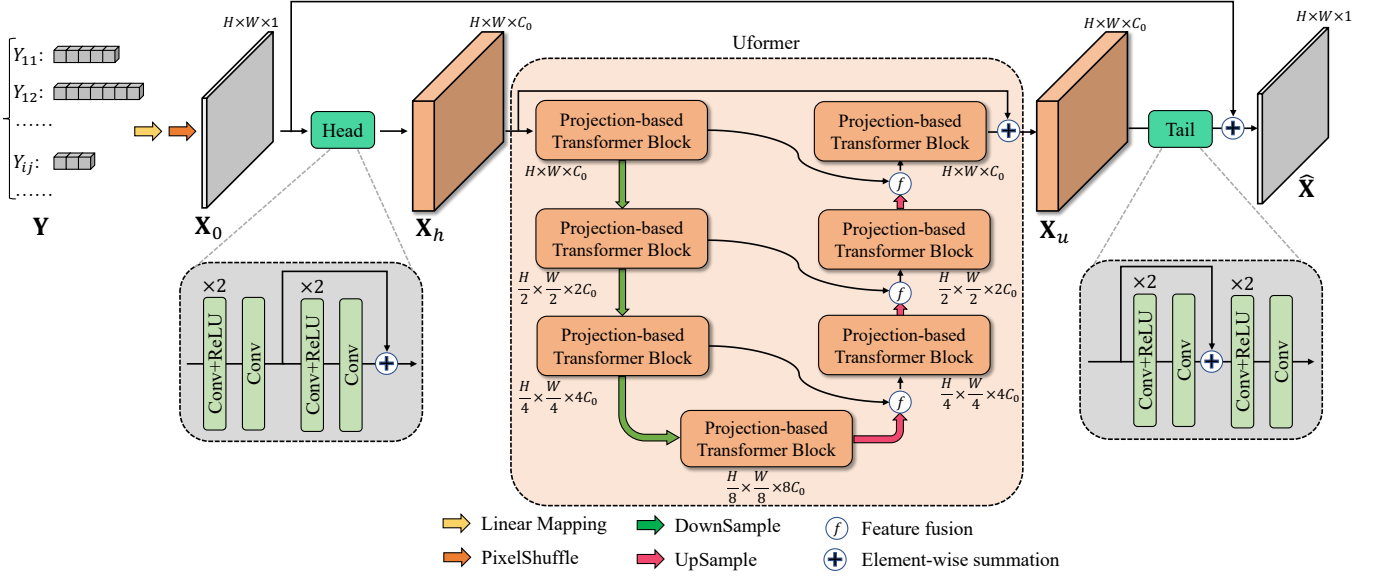


Fig. 4. Overview of the reconstruction model of the proposed Uformer-ICS. Given the adaptive sampling result  $\mathbf{Y}$ , the reconstruction model first applies linear mapping and pixel shuffle operations to it, and then feeds the obtained initialization  $\mathbf{X}_0$  into the *Head* module for extracting shallow features  $\mathbf{X}_h$ . Taking  $\mathbf{X}_h$  as input, the *Uformer* module captures the long-range dependencies to enhance the feature representation and outputs  $\mathbf{X}_u$ . Finally, the *Tail* module generates the final reconstruction result  $\hat{\mathbf{X}}$  by adding the initialization  $\mathbf{X}_0$  and aggregation features of  $\mathbf{X}_u$ .

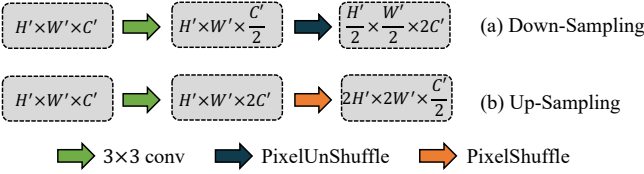


Fig. 5. Illustrations of the feature down-sampling and up-sampling operations.

self-attention in non-overlapping windows and its computational complexity increases linearly with image size. Given an input feature map  $\mathbf{Z} \in \mathbb{R}^{H' \times W' \times d}$ , the W-MSA divides it into non-overlapping windows of size  $W \times W \times d$ . Suppose that  $\mathbf{P} \in \mathbb{R}^{W^2 \times d}$  denotes the  $W^2$  pixels in a window, the W-MSA applies the self-attention process to these pixels as follows:

$$\mathbf{Q}, \mathbf{K}, \mathbf{V} = \mathbf{P}\mathbf{W}_q, \mathbf{P}\mathbf{W}_k, \mathbf{P}\mathbf{W}_v, \quad \text{Attention}(\mathbf{Q}, \mathbf{K}, \mathbf{V}) = \text{SoftMax}\left(\frac{\mathbf{Q}\mathbf{K}^T}{\sqrt{d}} + \mathbf{B}\right)\mathbf{V}, \quad (11)$$

where  $\mathbf{W}_q, \mathbf{W}_k, \mathbf{W}_v \in \mathbb{R}^{d \times d}$  are the *query*, *key*, and *value* projection matrices, respectively,  $\mathbf{Q}, \mathbf{K}, \mathbf{V}$  denote the *query*, *key* and *value* results, respectively, and  $\mathbf{B} \in \mathbb{R}^{(2W^2-1) \times (2W^2-1)}$  denotes the learnable relative position bias. The attention results are transformed into a feature map with the same size as  $\mathbf{Z}$ . It should be noted that we omit the multi-head format in Eq. (11) for simplicity. Besides, we also use the shifted window partitioning scheme [28] to capture dependencies across windows, and the W-MSA with shifted window partitioning is referred to SW-MSA.

3) *Projection-Based Transformer Block*: The projection operation can well utilize the prior knowledge of CS during the reconstruction process. It is necessary to integrate this CS characteristic into the transformer for achieving a high performance. As shown in Eq. (3), the projection operation updates each image block with a single channel. However, the features in a transformer architecture generally have smaller

resolutions but more channels than the input single-channel image. Therefore, the projection operation cannot be directly applied to the transformer architecture.

To address this issue, we propose a multi-channel projection, which is derived from the original projection operation expressed in Eq. (3) and shown in Fig. 6. We first reshape the input feature using the pixel shuffle operation [30], ensuring that it has the same resolution as the input image. We then use a  $3 \times 3$  convolutional layer to reduce the channel number to 1 and obtain a single-channel feature  $\mathbf{X}'$ . Thereafter, we apply block-wised projection to each block of the single-channel feature using the learnable measurement matrix  $\Phi$  and the adaptive sampling results  $\mathbf{Y}$ . The block-wise projection operation is calculated as follows:

$$\mathfrak{T}(\mathbf{x}_{ij}'') = \mathfrak{T}(\mathbf{x}_{ij}') + \alpha \Phi[1 : m_{ij}, :]^T (\mathbf{y}_{ij} - \Phi[1 : m_{ij}, :] \mathfrak{T}(\mathbf{x}_{ij}')), \quad (12)$$

where  $\mathfrak{T}(\mathbf{x}_{ij}')$  denotes the 1D vector form of each block  $\mathbf{x}_{ij}'$  in  $\mathbf{X}'$ ,  $m_{ij}$  denotes the measurement number of each block  $\mathbf{x}_{ij}'$ , and  $\alpha$  is set to be learnable. By combining and reshaping the block-wise projection results, we can also obtain a single-channel feature  $\mathbf{X}''$ . Finally, we successively apply a  $3 \times 3$  convolutional layer and the pixel unshuffle operation to  $\mathbf{X}''$  for restoring its channel number and original resolution.

After constructing the multi-channel projection for the transformer architecture, we develop a projection-based transformer block by directly integrating the multi-channel projection into the transformer architecture. Fig. 7 shows the structure of the projection-based transformer block. Given the input feature  $\mathbf{X}'$ , the entire process of the projection-based transformer block can be formulated as

$$\begin{aligned} \mathbf{Z}^{(0)} &= \mathbf{X}' \\ \mathbf{Z}^{(k)} &= \text{WTB}(\mathbf{Z}^{(k-1)}), \quad k = 1, \dots, L \\ \mathbf{X}'' &= \text{MC-Proj}(\text{LN}(\mathbf{Z}^{(L)})) \end{aligned} \quad (13)$$

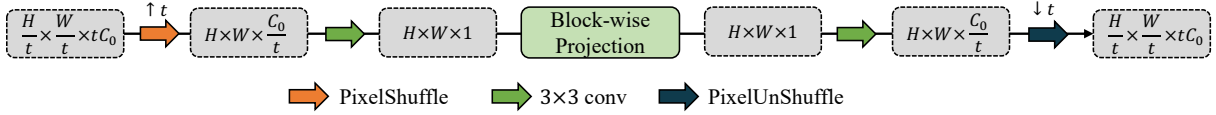


Fig. 6. Illustration of the multi-channel projection operation.

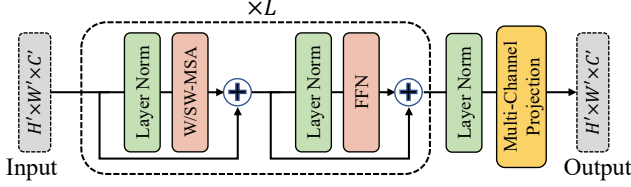


Fig. 7. Structure of the projection-based transformer block. First,  $L$  Transformer blocks are stacked to learn long-range dependencies, and then the multi-channel projection is used to update the features block-wise.

where LN represents the layer normalization [33], MC-Proj denotes the multi-channel projection, and WTB indicates the following calculation process of an original transformer block:

$$\begin{aligned} \mathbf{T}^{(k)} &= \mathbf{Z}^{(k-1)} + \text{W/SW-MSA}(\text{LN}(\mathbf{Z}^{(k-1)})) \\ \mathbf{Z}^{(k)} &= \mathbf{T}^{(k)} + \text{FFN}(\text{LN}(\mathbf{T}^{(k)})) \end{aligned} \quad (14)$$

where FFN denotes a feed-forward network containing two fully connected layers. Following the shifted window partitioning scheme [28], the W-MSA is used when  $k$  is odd and SW-MSA is used when  $k$  is even. Because the multi-channel projection reuses the learnable measurement matrix and only introduces two convolutional layers with small channel numbers, the projection-based transformer block can exploit the prior knowledge of CS with a small computation overhead and little extra parameters compared to the original stacked transformer blocks.

4) *Feature Fusion*: The encoder features are fused on the decoder side to enhance the feature representation. Given two features of the same size, they are directly concatenated in the channel dimension and a  $1 \times 1$  convolutional layer is used to reduce the number of channels in the concatenation result by 50%. Thereafter, a residual convolutional block is employed to further improve the feature fusion ability. Therefore, the feature fusion result has the same size as each input feature.

### E. Loss Function

Following the settings of existing CS methods [9], [11], we also use the mean square error (MSE) to calculate the loss. The loss function of the proposed model comprises three parts  $\mathcal{L}_1$ ,  $\mathcal{L}_2$  and  $\mathcal{L}_3$ . Let  $\{\mathbf{X}_k\}_{k=1}^N$  represent a training set. We first use the MSE to measure the difference between the input images and their corresponding reconstructed images as follows:

$$\mathcal{L}_1 = \frac{1}{2N} \sum_{k=1}^N \|\hat{\mathbf{X}}_k - \mathbf{X}_k\|_2^2, \quad (15)$$

where  $\hat{\mathbf{X}}_k$  denotes the reconstructed image of the  $k$ -th input image  $\mathbf{X}_k$ . Inspired by the cycle-consistent loss [36], we also use the MSE to measure the difference between the

measurements of the input images and the measurements of their corresponding reconstructed images as follows:

$$\mathcal{L}_2 = \frac{1}{2N} \sum_{k=1}^N \sum_{i=1}^h \sum_{j=1}^w \|y_{kij} - \Phi[1 : \mathbf{m}_{kij}, :] \mathfrak{T}(\hat{\mathbf{x}}_{kij})\|_2^2, \quad (16)$$

where  $\mathfrak{T}(\hat{\mathbf{x}}_{kij})$  denotes the 1D vector form of the image block  $\hat{\mathbf{x}}_{kij}$  in the reconstructed image  $\hat{\mathbf{X}}_k$ . Because a better initial reconstruction quality can lead to a higher training efficiency and better final reconstruction quality [37], we further add a regularization loss to enhance the initial reconstruction quality as follows:

$$\mathcal{L}_3 = \frac{1}{2N} \sum_{k=1}^N \|\hat{\mathbf{X}}_{k0} - \mathbf{X}_k\|_2^2, \quad (17)$$

where  $\hat{\mathbf{X}}_{k0}$  is the initial reconstruction result of the  $k$ -th input image  $\mathbf{X}_k$ . Finally, we define the total loss as:

$$\mathcal{L} = \mathcal{L}_1 + \mathcal{L}_2 + \lambda \mathcal{L}_3 \quad (18)$$

where  $\lambda$  is the regularization weight, which is set to 0.1 by default.

## IV. PERFORMANCE EVALUATION

### A. Experimental Settings

1) *Datasets*: Compared to pure CNN models, a transformer model needs to be trained using a much larger training set [15]. To thoroughly evaluate the performance of the proposed model, we randomly select 40000 images from the COCO 2017 Unlabeled Images dataset<sup>1</sup> [38] as the training dataset. We conduct experiments to evaluate all the CS methods over five commonly used datasets: Set5 [39], Set11 [25], Set14 [40], BSD100 [41], and Urban100 [42]. For the training and test datasets, we only utilize the Y channel in the YCbCr color space of each color image.

2) *Implementation Details*: The image block size in the sampling process is set to  $B = 32$ . The number of channels in  $\mathbf{X}_h$  is set to  $C_0 = 32$ . From the top to the bottom levels of the Uformer, the number  $L$  of the attention layers and FFN layers in the projection-based transformer block are set as [4, 4, 6, 6], and the number of heads in W/SW-MSA are set as [1, 2, 4, 8]. The window size in W/SW-MSA are set to 8 for all levels of the Uformer.

We train the proposed Uformer-ICS for 25 epochs at each sampling ratio. The batch size is set to 1. For each input image in the training process, we first randomly flip and rotate it to augment the image features and then randomly crop the augmentation result into a sub-image of size  $256 \times 256$  for training. We use the Adam optimizer [43] to optimize the parameters. The learning rate is initialized at 0.0001 and then

<sup>1</sup><https://cocodataset.org>

TABLE I  
 QUANTITATIVE PERFORMANCE COMPARISONS OF THE PROPOSED UFORMER-ICS AND UFORMER-ICS<sup>+</sup> WITH EXISTING CS METHODS UNDER MULTIPLE SAMPLING RATIOS ( $sr$ ). THE BEST AND SECOND BEST PSNR AND STRUCTURAL SIMILARITY INDEX MEASURE (SSIM) SCORES ARE HIGHLIGHTED IN RED AND BLUE, RESPECTIVELY.

Dataset	Methods	$sr$ (PSNR/SSIM)				
		0.01	0.04	0.1	0.25	0.5
Set5	TV [6]	16.84/0.4412	21.34/0.5554	25.88/0.7239	30.96/0.8712	36.22/0.9465
	BCS-FOCUSS [8]	16.79/0.4787	23.13/0.6549	27.30/0.7658	31.84/0.8693	36.26/0.9340
	BM3D-DAMP [23]	6.48/0.0080	14.70/0.4573	24.11/0.6849	31.24/0.8752	37.89/0.9461
	MH-BCS-SPL [34]	14.59/0.3812	24.10/0.6709	28.66/0.8108	32.94/0.8975	36.99/0.9467
	SCSNet [10]	23.39/0.6419	27.91/0.8225	32.74/0.9068	36.52/0.9505	41.54/0.9784
	CSNet <sup>+</sup> [9]	24.18/0.6470	27.47/0.7589	32.59/0.9062	36.74/0.9519	41.79/0.9803
	DPA-Net [12]	20.88/0.5877	27.27/0.8042	30.98/0.8875	35.55/0.9441	39.81/0.9733
	OPINE-Net [13]	22.42/0.6075	28.55/0.8351	33.14/0.9193	37.43/0.9590	42.22/0.9815
	ISTA-Net <sup>++</sup> [35]	19.71/0.5039	24.97/0.7270	29.60/0.8583	34.36/0.9315	38.61/0.9674
	AMP-Net [11]	23.48/0.6518	29.00/0.8359	33.42/0.9140	38.03/0.9586	42.72/0.9818
	<b>Uformer-ICS<sup>+</sup></b>	<b>24.99/0.6964</b>	<b>31.00/0.8595</b>	<b>35.17/0.9240</b>	<b>40.32/0.9668</b>	<b>45.69/0.9876</b>
<b>Uformer-ICS</b>	<b>24.56/0.7184</b>	<b>30.94/0.8728</b>	<b>34.95/0.9289</b>	<b>40.03/0.9651</b>	<b>45.58/0.9848</b>	
Set11	TV [6]	15.49/0.3800	19.25/0.4988	22.78/0.6592	27.64/0.8296	32.81/0.9264
	BCS-FOCUSS [8]	17.58/0.4488	20.96/0.5856	24.06/0.7075	28.41/0.8359	33.17/0.9203
	BM3D-DAMP [23]	5.18/0.0076	13.84/0.3904	21.21/0.6070	28.29/0.8484	35.19/0.9429
	MH-BCS-SPL [34]	12.82/0.3205	21.49/0.6218	26.01/0.7862	30.53/0.8891	34.94/0.9447
	SCSNet [10]	21.05/0.5573	25.05/0.7535	28.45/0.8612	32.63/0.9303	38.20/0.9745
	CSNet <sup>+</sup> [9]	21.02/0.5566	23.83/0.6918	28.34/0.8580	32.75/0.9304	38.52/0.9749
	DPA-Net [12]	18.20/0.5101	24.26/0.7541	27.66/0.8530	32.38/0.9311	36.80/0.9685
	OPINE-Net [13]	20.02/0.5362	25.52/0.7879	29.81/0.8904	34.81/0.9514	40.19/0.9800
	ISTA-Net <sup>++</sup> [35]	18.29/0.4585	22.91/0.6785	27.54/0.8351	32.70/0.9266	37.47/0.9667
	AMP-Net [11]	20.20/0.5581	25.26/0.7722	29.40/0.8779	34.63/0.9481	40.33/0.9804
	<b>Uformer-ICS<sup>+</sup></b>	<b>21.68/0.5827</b>	<b>26.77/0.7790</b>	<b>31.11/0.8838</b>	<b>36.42/0.9522</b>	<b>41.69/0.9798</b>
<b>Uformer-ICS</b>	<b>22.51/0.6293</b>	<b>27.59/0.8198</b>	<b>31.70/0.9055</b>	<b>36.87/0.9579</b>	<b>42.09/0.9802</b>	
Set14	TV [6]	17.01/0.4025	20.82/0.5008	24.32/0.6456	28.48/0.7988	33.35/0.9071
	BCS-FOCUSS [8]	18.32/0.4586	21.99/0.5716	25.26/0.6816	29.01/0.8082	33.19/0.9023
	BM3D-DAMP [23]	6.17/0.0076	15.08/0.4032	22.73/0.5794	28.18/0.7630	34.29/0.8901
	MH-BCS-SPL [34]	14.36/0.3383	22.65/0.5878	26.63/0.7308	30.46/0.8489	34.49/0.9243
	SCSNet [10]	22.44/0.5632	25.84/0.7074	29.25/0.8196	32.85/0.9096	37.64/0.9622
	CSNet <sup>+</sup> [9]	22.83/0.5630	25.32/0.6630	29.13/0.8169	32.88/0.9066	37.89/0.9631
	DPA-Net [12]	19.85/0.5095	25.19/0.6879	27.98/0.7917	31.91/0.8935	36.45/0.9544
	OPINE-Net [13]	21.92/0.5405	26.11/0.7217	29.38/0.8354	33.73/0.9229	38.71/0.9678
	ISTA-Net <sup>++</sup> [35]	19.19/0.4526	23.37/0.6245	26.81/0.7584	31.10/0.8779	35.60/0.9457
	AMP-Net [11]	22.79/0.5751	26.67/0.7219	29.92/0.8312	34.31/0.9213	39.28/0.9684
	<b>Uformer-ICS<sup>+</sup></b>	<b>23.81/0.5965</b>	<b>28.23/0.7404</b>	<b>31.81/0.8472</b>	<b>36.53/0.9313</b>	<b>41.48/0.9714</b>
<b>Uformer-ICS</b>	<b>23.78/0.6104</b>	<b>28.21/0.7547</b>	<b>31.63/0.8534</b>	<b>36.38/0.9335</b>	<b>41.52/0.9699</b>	
BSD100	TV [6]	17.63/0.4174	21.26/0.5054	24.68/0.6249	27.93/0.7719	31.97/0.8920
	BCS-FOCUSS [8]	19.10/0.4587	22.89/0.5625	25.25/0.6566	28.22/0.7795	31.86/0.8834
	BM3D-DAMP [23]	6.79/0.0065	15.84/0.4096	23.06/0.5513	26.97/0.6979	31.02/0.8265
	MH-BCS-SPL [34]	15.38/0.3614	23.15/0.5645	25.72/0.6754	28.98/0.8049	32.65/0.9004
	SCSNet [10]	23.79/0.5496	26.31/0.6733	28.61/0.7860	31.81/0.8925	36.50/0.9615
	CSNet <sup>+</sup> [9]	23.76/0.5484	25.61/0.6416	28.53/0.7834	31.75/0.8885	36.68/0.9618
	DPA-Net [12]	20.55/0.4952	24.94/0.6412	26.99/0.7431	30.36/0.8610	34.46/0.9414
	OPINE-Net [13]	21.90/0.5002	25.00/0.6675	27.55/0.7906	31.21/0.8984	36.03/0.9628
	ISTA-Net <sup>++</sup> [35]	19.98/0.4487	23.26/0.5869	25.86/0.7169	29.48/0.8535	33.97/0.9412
	AMP-Net [11]	23.45/0.5540	26.35/0.6807	28.87/0.7919	32.69/0.9032	37.71/0.9671
	<b>Uformer-ICS<sup>+</sup></b>	<b>23.88/0.5696</b>	<b>27.29/0.7078</b>	<b>30.67/0.8201</b>	<b>35.62/0.9227</b>	<b>41.53/0.9753</b>
<b>Uformer-ICS</b>	<b>23.63/0.5719</b>	<b>27.16/0.7051</b>	<b>29.99/0.8125</b>	<b>34.59/0.9159</b>	<b>41.00/0.9702</b>	
Urban100	TV [6]	16.17/0.3819	19.31/0.4766	22.07/0.6181	26.05/0.7889	31.06/0.9107
	BCS-FOCUSS [8]	16.68/0.4116	20.17/0.5279	22.89/0.6435	26.65/0.7864	31.19/0.8947
	BM3D-DAMP [23]	6.13/0.0065	14.36/0.3709	21.03/0.5650	27.05/0.7947	33.55/0.9194
	MH-BCS-SPL [34]	13.63/0.3177	20.63/0.5464	24.95/0.7399	29.63/0.8720	33.92/0.9380
	SCSNet [10]	20.63/0.5202	23.67/0.6851	26.65/0.8110	29.96/0.8987	34.66/0.9594
	CSNet <sup>+</sup> [9]	20.75/0.5204	22.78/0.6217	26.52/0.8053	30.19/0.8985	35.25/0.9621
	DPA-Net [12]	17.93/0.4664	23.23/0.6884	26.29/0.8082	30.61/0.9087	34.80/0.9602
	OPINE-Net [13]	20.03/0.5009	23.62/0.7104	27.28/0.8415	32.15/0.9310	37.29/0.9739
	ISTA-Net <sup>++</sup> [35]	17.48/0.4163	20.96/0.5990	24.66/0.7624	29.51/0.8942	34.41/0.9572
	AMP-Net [11]	20.90/0.5328	24.15/0.7029	27.38/0.8270	32.19/0.9258	37.51/0.9734
	<b>Uformer-ICS<sup>+</sup></b>	<b>20.49/0.5358</b>	<b>25.23/0.7236</b>	<b>29.03/0.8446</b>	<b>34.24/0.9336</b>	<b>39.96/0.9754</b>
<b>Uformer-ICS</b>	<b>22.34/0.6074</b>	<b>26.54/0.7859</b>	<b>30.11/0.8807</b>	<b>35.04/0.9460</b>	<b>40.06/0.9743</b>	

linearly decayed to 0.00001 during the training process. We use the TensorFlow framework to implement the proposed models, and conduct all the experiments on a computer with

two RTX3090 GPUs and an Intel i9-10920X CPU. It takes about 2.5 hours to train one epoch.



3) *Sampling and Reconstruction using One Model*: The proposed model can also sample and reconstruct images at arbitrary sampling ratios with only one-time training, which can significantly reduce the training time and storage burden. In our implementation, we term the proposed model with only one-time training for arbitrary sampling ratios as Uformer-ICS<sup>+</sup>. In the training process of Uformer-ICS<sup>+</sup>, each image in the training set is randomly assigned a target sampling ratio ranging from 0.01–0.5. We test the performances of both kinds of models in our experiments.

4) *Competing Methods*: We compare our method with six deep learning-based CS methods, which are developed using CNNs and have shown state-of-the-art reconstruction performances.

- SCSNet [10]: This is a scalable sampling network that utilizes only a single measurement matrix for multiple reconstruction models.
- CSNet<sup>+</sup> [9]: This is an end-to-end CS model that utilizes several residual convolutional blocks for image reconstruction.
- DPA-Net [12]: This method consists of a texture path and a structure path to reconstruct various image information and utilizes a texture attention module to bridge the information between two paths.
- OPINE-Net [13]: This method unfolds the traditional ISTA method [5] to construct an end-to-end multi-stage reconstruction network.
- ISTA-Net<sup>++</sup> [35]: This is also a scalable sampling network that uses multiple sampling matrices but only a single deep-unfolding multi-stage network.
- AMP-Net [11]: This is a deep-unfolding multi-stage network, which unfolds the traditional AMP method [22] and integrates deblocking modules to eliminate blocking artifacts.

Additionally, four traditional CS methods, the TV [6], BCS-FOCUSS [8], DAMP [23], and MH-BCS-SPL [34] are also compared to demonstrate the powerful learning ability of the deep learning-based CS methods. We evaluate all of these competing methods using their publicly available pre-trained models or implementation codes.

## B. Performance Evaluation

We compare the proposed method with other CS methods in terms of the quantitative results, visual results, and model complexity. The PSNR and SSIM scores are used to quantitatively evaluate the reconstruction quality.

1) *Quantitative Comparison*: We calculate the average PSNR and SSIM scores on the five testing datasets at the sampling ratios ranging from 0.01–0.5. Table I lists the experimental results for all competing CS methods. Benefiting from the powerful learning ability, all deep learning-based CS methods outperform the traditional CS methods. The proposed method achieves the best PSNR and SSIM scores for nearly all the sampling ratios. Specifically, the proposed Uformer-ICS can obtain significantly higher PSNR and SSIM scores than other deep learning-based methods on the Urban100 dataset, which contains high-resolution images with different

characteristics. The proposed Uformer-ICS can also achieve the best SSIM scores when the sampling ratio is smaller than 0.5.

Additionally, we also calculate the average PSNR scores over all the five testing datasets at all sampling ratios, and the results of these deep learning-based CS methods are shown in Fig. 1. It is evident that the proposed method achieve significantly higher scores than other deep learning-based methods for all sampling ratios. The quantitative comparison results presented in Table I and Fig. 1 indicate that the proposed method outperforms all other CS methods and has a better generalization ability for different datasets.

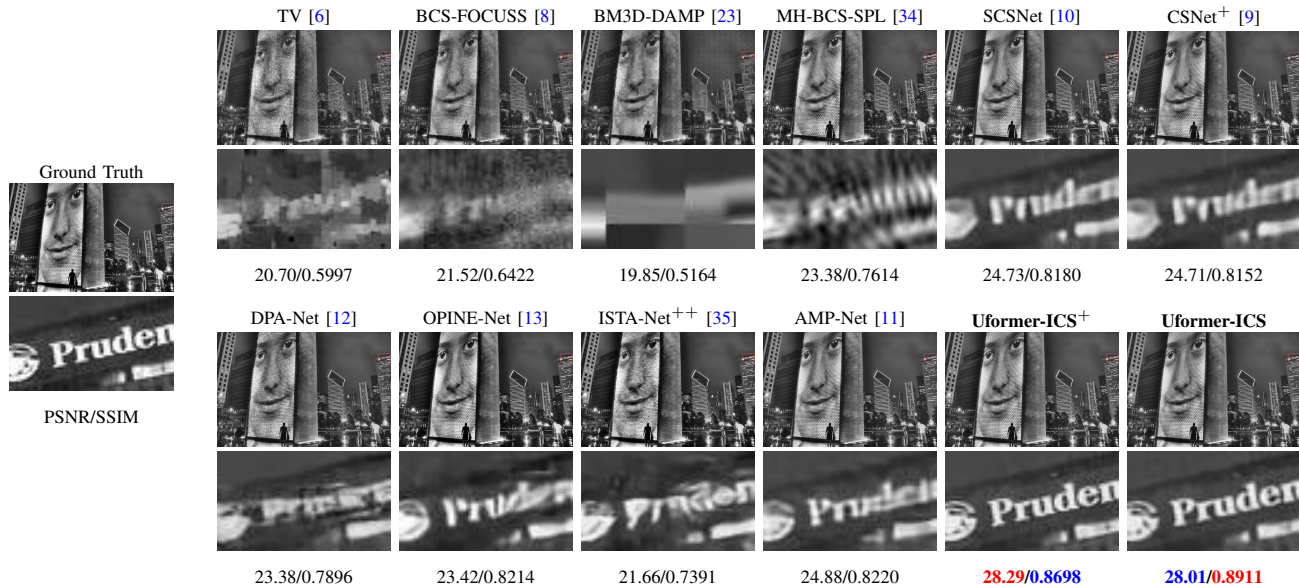
Regarding scalable sampling and reconstruction ability, the proposed Uformer-ICS<sup>+</sup> requires only one-time training but can sample and reconstruct images at arbitrary sampling ratios. Compared with the scalable CS methods SCSNet and ISTA-Net<sup>++</sup>, the proposed Uformer-ICS<sup>+</sup> can still obtain better PSNR and SSIM scores in most cases. For the test datasets Set5 and BSD100, the proposed Uformer-ICS<sup>+</sup> achieve the best PSNR scores compared to all other non-scalable deep learning-based CS methods. These comparison results demonstrate the tremendous potential of the proposed method for scalable sampling and reconstruction.

2) *Visual Comparison*: Fig. 8 shows the visual results of different CS methods at the sampling ratios of 0.04 and 0.1. The reconstruction results of all the traditional CS methods clearly show blocking artifacts, whereas those of the deep learning-based CS methods show significantly fewer blocking artifacts. Moreover, the visual results demonstrate that the proposed Uformer-ICS can recover more image details and clearer edges than other deep learning-based CS methods. For example, the reconstructed images of our Uformer-ICS exhibit more details around the letter area in the “ppt3” and “img-076” images. This is because the proposed sampling model uses an adaptive sampling strategy to allocate more sampling resources to the image block that has less sparsity, and the proposed reconstruction model can simultaneously capture the long-range dependency and local features of the image to reconstruct image information.

## C. Model Complexity

We test the average running times on different image resolutions to evaluate the actual reconstruction efficiencies of all competing CS methods. Specifically, we randomly select five images from the ImageNet validation dataset and resize them to  $128 \times 128$ ,  $256 \times 256$ ,  $512 \times 512$ , and  $1024 \times 1024$  using the bicubic interpolation algorithm. Thereafter, the average running times are calculated for the five images using these four kinds of image resolutions. Additionally, we utilize the number of floating-point operations (FLOPs) and parameters to theoretically quantify the time complexity of deep learning-based CS methods. It should be noted that we calculate the FLOPs on an input image of size  $256 \times 256$ . The traditional CS methods are tested on the CPU device, whereas the deep learning-based CS methods are tested on the GPU device.

Table II presents the comparison results of model complexity. All deep learning-based CS methods have better PSNR

(a) Reconstruction results of the image "ppt3" at  $sr = 0.04$ (b) Reconstruction results of the image "img-076" at  $sr = 0.1$ Fig. 8. Reconstruction results of various CS methods at sampling ratios ( $sr$ ) of 0.04 and 0.1.

scores and extremely faster speeds than traditional ones. Moreover, the running speeds of all deep learning-based CS methods are of the same order of magnitude. This is because the GPU device has a powerful computational ability and can run these deep learning-based models at a high speed. The proposed method can achieve the best PSNR scores for all the image resolutions. Despite the transformer architecture, the proposed method has only a little more model parameters than the DPA-Net [12]. Additionally, the Uformer-ICS<sup>+</sup> uses a single model for arbitrary sampling and reconstruction tasks, which can significantly reduce the number of parameters when

sampling at multiple sampling ratios is required. Thus, the proposed method can well balance the trade-off between model complexity and reconstruction performance. It achieves the best reconstruction performance while maintaining a modest model complexity.

#### D. Retraining Models At COCO Dataset

The proposed models are trained on the COCO dataset to explore the potential performance of the transformer architecture. For the compared deep learning-based CS methods, the SCSNet [10], CSNet<sup>+</sup> [9], and the AMP-Net [11] are

TABLE II

TIME COMPLEXITY COMPARISON BETWEEN DIFFERENT CS METHODS. THE AVERAGE PSNR SCORES AND RUNNING TIMES ARE LISTED FOR DIFFERENT IMAGE SIZES, AND THE FLOPS IS MEASURED ON AN IMAGE OF SIZE  $256 \times 256$ .

	Methods	PSNR (dB) / Times (s)				Scalable Sampling	Param.	FLOPs
		$128 \times 128$	$256 \times 256$	$512 \times 512$	$1024 \times 1024$			
Traditional CS methods	TV [6]	22.78/0.2059	24.62/0.6852	27.91/2.6385	32.44/9.9298	✓	-	-
	BM3D-DAMP [23]	21.67/3.3867	23.48/11.7512	26.98/43.9482	34.54/174.3528	✓	-	-
	MH-BCS-SPL [34]	22.89/0.6402	25.14/2.9934	29.70/20.6294	38.26/108.1546	✓	-	-
	BCS-FOCUSS [8]	22.63/1.2723	24.61/2.3107	28.78/7.4328	36.71/29.8565	✓	-	-
Deep learning-based CS methods	SCSNet [10]	25.00/0.0084	27.24/0.0084	32.77/0.0161	42.44/0.0642	✓	1.98M	<b>12.32</b>
	CSNet <sup>+</sup> [9]	24.94/ <b>0.0066</b>	27.17/0.0063	32.62/0.0180	41.85/0.0667	×	0.90M	24.29
	DPA-Net [12]	23.59/0.0190	25.94/0.0218	30.93/0.0550	39.76/0.3488	×	9.48M	53.07
	OPINE-Net [13]	25.07/0.0078	27.88/ <b>0.0062</b>	33.90/ <b>0.0065</b>	43.96/ <b>0.0129</b>	×	<b>0.79M</b>	36.01
	ISTA-Net <sup>++</sup> [35]	23.65/0.0194	26.27/0.0147	31.65/0.0143	38.36/0.0145	✓	1.05M	52.90
	AMP-Net [11]	25.27/0.0167	27.82/0.0169	33.93/0.0372	43.84/0.1318	×	0.93M	24.09
	<b>Uformer-ICS<sup>+</sup></b>	<b>25.63/0.0344</b>	28.26/0.0567	35.47/0.1859	45.01/0.6872	✓	9.58M	40.62
	<b>Uformer-ICS</b>	25.59/0.0344	<b>28.68/0.0567</b>	<b>35.66/0.1859</b>	<b>46.73/0.6872</b>	×	9.58M	40.62

TABLE III

QUANTITATIVE PSNR SCORE COMPARISONS BETWEEN THE PROPOSED AND RETRAINED CS METHODS UNDER MULTIPLE SAMPLING RATIOS ( $sr$ ). THE "TOTAL AVG." INDICATES THAT THE PSNR SCORES ARE AVERAGED OVER FIVE TEST DATASETS.

Dataset	$sr$	SCS	CS	DPA	OPIN	ISTA-	AMP	Uformer	Uformer
		Net <sup>+</sup> [10]	Net <sup>+</sup> [9]	-Net [12]	E-Net [13]	Net <sup>++</sup> [35]	-Net [11]		
Set5	0.01	23.16	23.88	21.69	23.11	19.39	23.12	24.99	24.56
	0.04	27.61	28.27	26.88	28.79	24.59	28.46	31.00	30.94
	0.1	31.99	32.31	30.55	33.14	29.03	32.88	35.17	34.95
	0.25	36.21	36.68	34.83	37.22	33.70	37.35	40.32	40.03
	0.5	40.79	41.23	38.53	41.71	37.33	42.14	45.69	45.58
Set11	0.01	21.14	20.98	18.71	19.96	18.27	19.94	21.68	22.51
	0.04	25.03	24.71	23.78	25.50	22.74	24.83	26.77	27.59
	0.1	28.50	28.31	27.16	29.44	27.31	29.09	31.11	31.70
	0.25	32.51	32.60	31.73	34.36	32.36	33.97	36.42	36.87
	0.5	37.69	37.98	35.73	39.36	36.81	39.59	41.69	42.09
Set14	0.01	22.51	22.65	20.56	22.48	19.08	22.55	23.81	23.78
	0.04	25.85	26.14	25.03	26.86	23.15	26.59	28.23	28.21
	0.1	29.14	29.13	27.68	29.93	26.51	29.85	31.81	31.63
	0.25	32.82	33.02	31.50	34.15	30.56	33.93	36.53	36.38
	0.5	37.33	37.35	35.32	39.01	34.68	38.85	41.48	41.52
BSD 100	0.01	23.81	23.69	21.48	23.01	19.92	23.12	23.88	23.63
	0.04	26.31	26.02	24.91	25.36	23.10	26.13	27.29	27.16
	0.1	28.55	28.31	26.93	28.73	25.69	28.72	30.67	29.99
	0.25	31.72	31.68	30.08	32.31	29.21	32.36	35.62	34.59
	0.5	36.33	36.16	33.78	37.11	33.36	37.25	41.52	41.00
Urban 100	0.01	20.67	20.69	18.87	20.71	17.40	20.78	20.49	22.34
	0.04	23.73	23.47	22.89	24.57	20.92	24.28	25.23	26.54
	0.1	26.76	26.27	25.75	28.31	24.68	27.44	29.03	30.11
	0.25	30.32	29.97	30.17	33.27	29.48	32.16	34.24	35.04
	0.5	34.96	34.25	33.98	38.46	34.06	37.60	39.96	40.06
Total Avg.	0.01	22.22	22.20	20.16	21.84	18.68	21.91	22.32	23.04
	0.04	25.13	24.91	24.02	25.62	22.17	25.34	26.51	27.06
	0.1	27.88	27.56	26.55	28.75	25.45	28.34	30.15	30.33
	0.25	31.31	31.17	30.39	33.04	29.66	32.55	35.22	35.12
	0.5	35.96	35.60	34.16	38.02	34.00	37.78	40.94	40.78

trained on the BSD500 dataset [41]; the DPA-Net [12] and the OPINE-Net [13] are trained on the T91 dataset [44]; and the ISTA-Net<sup>++</sup> is trained on the Train400 dataset. To evaluate the performances of these deep learning-based methods on the larger training set, we retrain them on the COCO dataset and their new performances are listed in Table III. It can be seen that in most cases, the proposed method can still obtain better

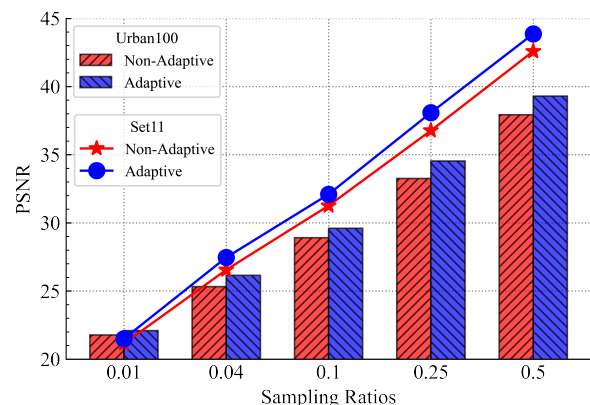


Fig. 9. Comparison results between the adaptive sampling and the non-adaptive sampling schemes for the proposed Uformer-ICS on Set11 and Urban100 datasets.

reconstruction performance than other deep learning-based CS methods under the same training set.

## V. ABLATION STUDIES

In this section, we conduct ablation studies on several components of the proposed Uformer-ICS to investigate their effectiveness. The reconstruction results are obtained from the models that are trained for the first 10 epochs.

1) *Adaptive Sampling*: A natural image usually contains different sparsities in different image blocks. To retain more information of the original image in the compressed measurements, we use an adaptive sampling strategy to sample image blocks based on their sparsity, which is estimated using their saliency information. An image block with a higher sparsity is allocated fewer sampling resources, and vice versa. To demonstrate the effectiveness of the adaptive sampling strategy, we design a new model by discarding the adaptive sampling strategy from the proposed Uformer-ICS and train it by sampling each image block equally. Fig. 9 shows the testing results of the new model on Set11 and Urban100 datasets. It is evident that the Uformer-ICS can obtain better PSNR scores under all sampling ratios than the new model, which confirms the positive effects of the adaptive sampling strategy for image reconstruction.

TABLE IV  
 ABLATION STUDY RESULTS OF THE PROPOSED UFORMER-ICS ON SET11 AND URBAN100 DATASETS AT DIFFERENT SAMPLING RATIOS ( $sr$ ). FOR THE FEATURE FUSION, ‘‘CONCAT’’ DENOTES THE CONCATENATION OPERATION AND ‘‘ADD’’ INDICATES THE SKIP CONNECTION.

Setting	Multi-Channel Projection	Feature Fusion	Set11					Urban100					Parameters
			$sr$					$sr$					
			0.01	0.04	0.1	0.25	0.5	0.01	0.04	0.1	0.25	0.5	
(a)	×	‘‘concat’’	22.07	24.03	27.41	32.50	38.64	21.77	22.89	25.25	29.22	34.90	9.575M
(b)	✓	‘‘add’’	22.34	<b>27.56</b>	31.44	36.30	41.55	<b>22.10</b>	26.13	<b>29.65</b>	34.50	39.25	9.534M
(c)	✓	‘‘concat’’	<b>22.41</b>	27.52	<b>31.53</b>	<b>36.33</b>	<b>41.60</b>	22.09	<b>26.15</b>	29.60	<b>34.54</b>	<b>39.30</b>	9.577M

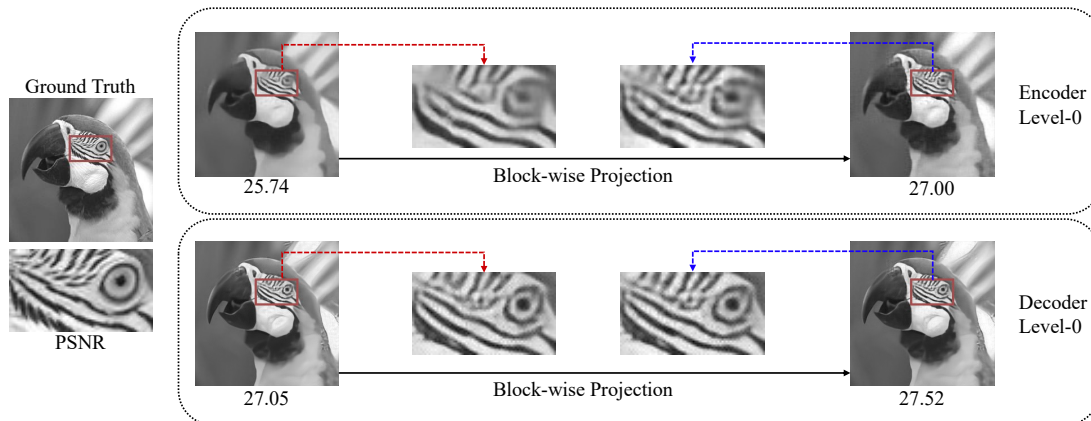


Fig. 10. Visual effects of the feature maps in the multi-channel projection modules of the proposed Uformer-ICS. The sampling ratio is set to 0.04.

### A. Multi-Channel Projection

For the proposed reconstruction model, we construct the Uformer architecture to utilize the long-range dependency capture ability of the transformer. Considering that CS characteristics are crucial for image reconstruction in CS tasks [11], [13], we develop a projection-based Transformer block to introduce the prior projection knowledge of CS into the transformer architecture. As shown in Fig. 7, we integrate the multi-channel projection into the original stacked Transformer blocks to construct the projection-based transformer block. Because the multi-channel projection reuses the measurement matrix and the measurements to update the image block, it can introduce the CS characteristics into the transformer architecture. Additionally, it brings in little computation overhead and few extra parameters by using only two low-channel convolutional layers. As can be seen from the settings (a) and (c) in Table IV, the multi-channel projection only increases the model parameters from 9.575M to 9.577M.

To evaluate the effectiveness of the multi-channel projection, we remove all the multi-channel projection operations in the projection-based transformer block to test the reconstruction performance. As shown in Table IV, without the multi-channel projection operations, the PSNR scores will drop by approximately 0.3~3 dB and 0.3~5 dB on Set11 and Urban100 datasets, respectively, thereby demonstrating the importance of our multi-channel projection for image reconstruction. In addition, Fig. 10 presents the visualization results of the feature maps in the multi-channel projection modules of the proposed Uformer-ICS. The sampling ratio is set to 0.04. It can be observed that the projection results have finer details and clearer edges than the input feature maps. The quantitative results in Table IV and the visual results in Fig. 10

verify the effectiveness of the multi-channel projection.

### B. Feature Fusion

In the proposed model, we use the concatenation operation for feature fusion to aggregate the encoder features on the decoder side. In addition to the concatenation operation, another commonly used feature fusion method is the skip connection [31], which directly adds the features of the two input branches element-wise. As can be seen from Table IV, the concatenation operation and skip connection have little difference on the reconstruction performance. In this study, we use the concatenation operation for feature fusion by default.

## VI. CONCLUSION

In this study, we proposed a novel transformer-based network for image CS, called the Uformer-ICS. Inspired by the development of the vision transformers, we developed a new usage of the transformer to make it suitable for CS tasks. Specifically, we first constructed a multi-channel projection and then developed a projection-based transformer block by integrating the multi-channel projection into the original stacked transformer blocks. This allows the proposed transformer architecture to use the prior projection knowledge of CS with a small computation overhead and few extra parameters. Compared with existing CNN-based CS methods, the proposed method can utilize the transformer architecture to learn long-range dependencies, thereby obtaining a better feature representation ability. Moreover, considering that natural images may have an uneven sparsity distribution, we proposed an adaptive sampling strategy to adaptively sample images based on block sparsity. Experimental results verified the effectiveness of the proposed Uformer-ICS, showing that

it outperforms existing deep learning-based CS methods, and proved that it has tremendous potential for scalable sampling and reconstruction.

## REFERENCES

- [1] E. J. Candès, J. Romberg, and T. Tao, "Robust uncertainty principles: Exact signal reconstruction from highly incomplete frequency information," *IEEE Transactions on Information Theory*, vol. 52, no. 2, pp. 489–509, 2006.
- [2] D. L. Donoho, "Compressed sensing," *IEEE Transactions on Information Theory*, vol. 52, no. 4, pp. 1289–1306, 2006.
- [3] X. Yuan, D. J. Brady, and A. K. Katsaggelos, "Snapshot compressive imaging: Theory, algorithms, and applications," *IEEE Signal Processing Magazine*, vol. 38, no. 2, pp. 65–88, 2021.
- [4] L. Gong, K. Qiu, C. Deng, and N. Zhou, "An optical image compression and encryption scheme based on compressive sensing and rsa algorithm," *Optics and Lasers in Engineering*, vol. 121, pp. 169–180, 2019.
- [5] A. Beck and M. Teboulle, "A fast iterative shrinkage-thresholding algorithm for linear inverse problems," *SIAM Journal on Imaging Sciences*, vol. 2, no. 1, p. 183–202, 2009.
- [6] C. Li, W. Yin, and Y. Zhang, "User's guide for tval3: Tv minimization by augmented lagrangian and alternating direction algorithms," *CAAM report*, vol. 20, no. 46-47, p. 4, 2009.
- [7] Lu Gan, "Block compressed sensing of natural images," in *2007 15th International Conference on Digital Signal Processing*, 2007, pp. 403–406.
- [8] A. S. Unde and P. Deepthi, "Block compressive sensing: Individual and joint reconstruction of correlated images," *Journal of Visual Communication and Image Representation*, vol. 44, pp. 187–197, 2017.
- [9] W. Shi, F. Jiang, S. Liu, and D. Zhao, "Image compressed sensing using convolutional neural network," *IEEE Transactions on Image Processing*, vol. 29, pp. 375–388, 2020.
- [10] —, "Scalable convolutional neural network for image compressed sensing," in *2019 IEEE/CVF Conference on Computer Vision and Pattern Recognition (CVPR)*, 2019, pp. 12 282–12 291.
- [11] Z. Zhang, Y. Liu, J. Liu, F. Wen, and C. Zhu, "Amp-net: Denoising-based deep unfolding for compressive image sensing," *IEEE Transactions on Image Processing*, vol. 30, pp. 1487–1500, 2021.
- [12] Y. Sun, J. Chen, Q. Liu, B. Liu, and G. Guo, "Dual-path attention network for compressed sensing image reconstruction," *IEEE Transactions on Image Processing*, vol. 29, pp. 9482–9495, 2020.
- [13] J. Zhang, C. Zhao, and W. Gao, "Optimization-inspired compact deep compressive sensing," *IEEE Journal of Selected Topics in Signal Processing*, vol. 14, no. 4, pp. 765–774, 2020.
- [14] A. Vaswani, N. Shazeer, N. Parmar, J. Uszkoreit, L. Jones, A. N. Gomez, E. Kaiser, and I. Polosukhin, "Attention is all you need," *Advances in neural information processing systems*, vol. 30, 2017.
- [15] A. Dosovitskiy, L. Beyer, A. Kolesnikov, D. Weissenborn, X. Zhai, T. Unterthiner, M. Dehghani, M. Minderer, G. Heigold, S. Gelly, J. Uszkoreit, and N. Houlsby, "An image is worth 16x16 words: Transformers for image recognition at scale," 2021.
- [16] N. Carion, F. Massa, G. Synnaeve, N. Usunier, A. Kirillov, and S. Zagoruyko, "End-to-end object detection with transformers," in *European Conference on Computer Vision*, 2020, pp. 213–229.
- [17] F. Yang, H. Yang, J. Fu, H. Lu, and B. Guo, "Learning texture transformer network for image super-resolution," in *Proceedings of the IEEE/CVF Conference on Computer Vision and Pattern Recognition*, 2020, pp. 5791–5800.
- [18] J. Liang, J. Cao, G. Sun, K. Zhang, L. Van Gool, and R. Timofte, "Swinir: Image restoration using swin transformer," in *Proceedings of the IEEE/CVF International Conference on Computer Vision*, 2021, pp. 1833–1844.
- [19] Y. Yu, B. Wang, and L. Zhang, "Saliency-Based Compressive Sampling for Image Signals," *IEEE Signal Processing Letters*, vol. 17, no. 11, pp. 973–976, Nov. 2010.
- [20] J. E. Fowler, S. Mun, and E. W. Tramel, "Multiscale block compressed sensing with smoothed projected Landweber reconstruction," in *2011 19th European Signal Processing Conference*, 2011, pp. 564–568.
- [21] J. Chen, X. Zhang, and H. Meng, "Self-adaptive sampling rate assignment and image reconstruction via combination of structured sparsity and non-local total variation priors," *Digital Signal Processing*, vol. 29, pp. 54–66, Jun. 2014.
- [22] D. L. Donoho, A. Maleki, and A. Montanari, "Message-passing algorithms for compressed sensing," *Proceedings of the National Academy of Sciences*, vol. 106, no. 45, pp. 18 914–18 919, 2009.
- [23] C. A. Metzler, A. Maleki, and R. G. Baraniuk, "From denoising to compressed sensing," *IEEE Transactions on Information Theory*, vol. 62, no. 9, pp. 5117–5144, 2016.
- [24] A. Mousavi, A. B. Patel, and R. G. Baraniuk, "A Deep Learning Approach to Structured Signal Recovery," *2015 53rd Annual Allerton Conference on Communication, Control, and Computing (Allerton)*, pp. 1336–1343, 2015.
- [25] K. Kulkarni, S. Lohit, P. Turaga, R. Kerviche, and A. Ashok, "Reconnet: Non-iterative reconstruction of images from compressively sensed measurements," in *2016 IEEE Conference on Computer Vision and Pattern Recognition (CVPR)*, 2016, pp. 449–458.
- [26] W. Shi, F. Jiang, S. Zhang, and D. Zhao, "Deep networks for compressed image sensing," in *2017 IEEE International Conference on Multimedia and Expo (ICME)*, 2017, pp. 877–882.
- [27] J. Zhang and B. Ghanem, "Ista-net: Interpretable optimization-inspired deep network for image compressive sensing," in *2018 IEEE Conference on Computer Vision and Pattern Recognition (CVPR)*, 2018, pp. 1828–1837.
- [28] Z. Liu, Y. Lin, Y. Cao, H. Hu, Y. Wei, Z. Zhang, S. Lin, and B. Guo, "Swin Transformer: Hierarchical Vision Transformer using Shifted Windows," *arXiv:2103.14030 [cs]*, Aug. 2021.
- [29] S. W. Zamir, A. Arora, S. Khan, M. Hayat, F. S. Khan, and M.-H. Yang, "Restormer: Efficient transformer for high-resolution image restoration," *arXiv preprint arXiv:2111.09881*, 2021.
- [30] W. Shi, J. Caballero, F. Huszár, J. Totz, A. P. Aitken, R. Bishop, D. Rueckert, and Z. Wang, "Real-time single image and video super-resolution using an efficient sub-pixel convolutional neural network," in *Proceedings of the IEEE Conference on Computer Vision and Pattern Recognition*, 2016, pp. 1874–1883.
- [31] K. He, X. Zhang, S. Ren, and J. Sun, "Deep residual learning for image recognition," in *Proceedings of the IEEE Conference on Computer Vision and Pattern Recognition*, 2016, pp. 770–778.
- [32] O. Ronneberger, P. Fischer, and T. Brox, "U-net: Convolutional networks for biomedical image segmentation," in *International Conference on Medical Image Computing and Computer-Assisted Intervention*, 2015, pp. 234–241.
- [33] J. L. Ba, J. R. Kiros, and G. E. Hinton, "Layer normalization," *arXiv preprint arXiv:1607.06450*, 2016.
- [34] C. Chen, E. W. Tramel, and J. E. Fowler, "Compressed-sensing recovery of images and video using multihypothesis predictions," in *2011 Conference Record of the Forty Fifth Asilomar Conference on Signals, Systems and Computers (ASILOMAR)*, 2011, pp. 1193–1198.
- [35] D. You, J. Xie, and J. Zhang, "Ista-net++: Flexible deep unfolding network for compressive sensing," in *2021 IEEE International Conference on Multimedia and Expo (ICME)*. IEEE, 2021, pp. 1–6.
- [36] J.-Y. Zhu, T. Park, P. Isola, and A. A. Efros, "Unpaired image-to-image translation using cycle-consistent adversarial networks," in *Proceedings of the IEEE international conference on computer vision*, 2017, pp. 2223–2232.
- [37] H. Yao, F. Dai, S. Zhang, Y. Zhang, Q. Tian, and C. Xu, "Dr2-net: Deep residual reconstruction network for image compressive sensing," *Neurocomputing*, vol. 359, pp. 483–493, 2019.
- [38] T.-Y. Lin, M. Maire, S. Belongie, J. Hays, P. Perona, D. Ramanan, P. Dollár, and C. L. Zitnick, "Microsoft COCO: Common Objects in Context," in *European Conference on Computer Vision*, 2014, pp. 740–755.
- [39] M. Bevilacqua, A. Roumy, C. Guillemot, and M. line Alberi Morel, "Low-complexity single-image super-resolution based on nonnegative neighbor embedding," in *Proceedings of the British Machine Vision Conference*, 2012, pp. 135.1–135.10.
- [40] R. Zeyde, M. Elad, and M. Protter, "On single image scale-up using sparse-representations," in *Curves and Surfaces*, 2012, pp. 711–730.
- [41] D. Martin, C. Fowlkes, D. Tal, and J. Malik, "A database of human segmented natural images and its application to evaluating segmentation algorithms and measuring ecological statistics," in *Proceedings Eighth IEEE International Conference on Computer Vision (ICCV)*, vol. 2, July 2001, pp. 416–423.
- [42] J.-B. Huang, A. Singh, and N. Ahuja, "Single image super-resolution from transformed self-exemplars," in *Proceedings of the IEEE Conference on Computer Vision and Pattern Recognition*, 2015, pp. 5197–5206.
- [43] D. P. Kingma and J. Ba, "Adam: A method for stochastic optimization," in *3rd International Conference on Learning Representations, ICLR 2015*, 2015.
- [44] C. Dong, C. C. Loy, K. He, and X. Tang, "Learning a deep convolutional network for image super-resolution," in *European Conference on Computer Vision*. Springer, 2014, pp. 184–199.